6
Bis(formazanate) Iron(II) Complexes as Cathode Material for One-Compartment H_2O_2 Fuel Cell

Research Article based on this study:

Birara, S., Majumder, M., Metre, R. K. Bis(formazanate) Iron(II) Complexes as Cathode Material for One-Compartment H_2O_2 Fuel Cell. Dalton Transactions, 2025, 54, 4120-4134.

6.1 Introduction

Despite being initially reported in the 1890s, formazans have only been widely investigated since the early 1940s [Nineham, 1955b]. In recent years, formazanates with tetraazapentadienyl cores (NNCNN) structurally related to β-diketiminates ligands have gained popularity as N-chelating ligands [Bourget-merle et al., 2002; Gilroy & Otten, 2020e]. The backbone of formazanates contains two additional nitrogen atoms than that of β-diketiminates, which gives them more accessible redox properties and stronger visible absorption since their LUMOs are more stabilized (Figure 6.1). Furthermore, the four nitrogen atoms in the backbone confer coordinative flexibility, enabling the formation of 4-, 5-, and 6-membered chelates.

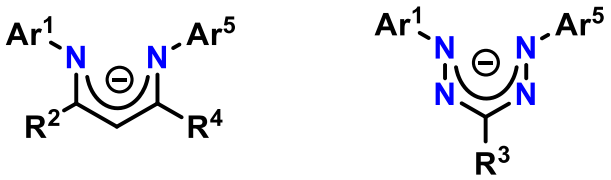


Figure 6.1. β-diketiminate ligand (left) and formazanate ligand (right).

The fact that they possess high-lying filled and low-lying empty orbitals of π-symmetry makes them suitable for both oxidative and reductive redox reactions. Since LUMOs have low energy compared to β-diketiminates and other related ligand families, formazanate metal complexes are likely to undergo ligand-based reduction reactions easily. As redox-active ligands can accept and donate electrons in a reversible manner, they offer a convenient method of generating more accessible reduced states, and by lowering their orbital energy, they can moderate the redox potential [Luca & Crabtree, 2013; Lyaskovskyy & De Bruin, 2012]. The low-energy vacant ligand orbital adjacent to the metal facilitates the reduction of the complex. As evidenced by the literature, formazanates easily undergo ligand-centered reduction when attached to zinc, iron, and boron [Broere et al., 2018c; Chang et al., 2015d; Gilroy et al., 2007b]. Numerous elegant studies have corroborated the non-innocent redox nature of formazanates. Exploring the redox-active characteristics of the formazan ligands has led to the discovery of new potential applications in coordination chemistry. Formazanate metal complexes are being thoroughly researched about their potential for their usage in designing molecular magnets, as well as using their redox-active behavior in the field of catalysis [De Vries & Otten, 2022b; Milocco et al., 2020; Travieso-Puente et al., 2016c].

The formazanate ligand also exhibited non-innocent behavior in complexes with aluminum, copper, iron, ruthenium, and Group 14 elements (Si, Ge, Sn) [Ito et al., 2022; Maar et al., 2018]. A number of rare-earth complexes with various formazanate ligands have also been investigated for their redox properties [Jin et al., 2022a]. Various studies have demonstrated catalytic reactivity resulting from the redox non-innocence of the formazanate ligand, where a decisive redox step is determined by the ability of the ligand to store and release electrons reversibly. Otten et al. have developed a zinc formazanate complex that displays the redox activity of the formazanate ligand employed in catalysis [De Vries & Otten, 2022b]. Adhikari et al. reported an iron-formazanate molecule proficiently preparing α-keto amides, where the redox non-innocence of formazanate ligand governs the catalytic efficiency [V. Singh et al., 2022b]. During the past two decades, the coordination chemistry of formazans and formazanates has been revitalized due to their facile synthesis and unique properties. Our group recently utilized an ionic organotin complex based on formazan to construct a WORM-type memory device [Birara, Betal, et al., 2023b]. In addition, our research utilized a bis(formazanate) Zinc complex as the active material for constructing memory devices that exhibited non-volatile resistive random access memory (RRAM) characteristics [Birara, Saini, et al., 2023]. As part of our efforts to discover novel and unique properties associated with the redox-active formazanate complexes, we present herein the synthesis of formazanate-based iron complexes and the use of its redox-active moiety for the development of electroactive materials in single-compartment hydrogen peroxide fuel cells.

Since hydrogen peroxide (H_2O_2) is a high energy-density liquid with dual functionality as both fuel and oxidant, single-compartment hydrogen peroxide fuel cells have recently gained prominence as a platform for energy conversion [Mousavi Shaegh et al., 2012a; Sanli & Aytaç, 2011; Yamazaki et al., 2008; F. Yang et al., 2013]. Hydrogen peroxide fuel cells generate energy through the exergonic reactions of oxidizing hydrogen peroxide to oxygen and reducing hydrogen peroxide to water. Electrochemical conversion of energy contained in hydrogen peroxide into electrical energy can be achieved by performing these two half-reactions on an anode and a cathode, respectively. Eqs (a), (b), and (c) describe the reactions occurring at the anode and cathode of the H_2O_2 fuel cell.

$$\text{Cathode: } H_2O_2 + 2H^+ + 2e^- \rightarrow 2H_2O \text{ (1.78 V } \textit{vs.}\text{ NHE)} \quad \text{(a)}$$

$$\text{Anode: } H_2O_2 \rightarrow O_2 + 2H^+ + 2e^- \text{ (0.682 V } \textit{vs.}\text{ NHE)} \quad \text{(b)}$$

$$\text{Total: } H_2O_2 \rightarrow 2H_2O + O_2 \text{ (1.09 V)} \quad \text{(c)}$$

In the case where H_2O_2 is used as a fuel as well as an oxidant, the net reaction (Eqn c) that produces water and oxygen from peroxide has a net potential gain of 1.09 V, which is slightly lesser but closer to those of methanol and H_2 fuel cells. Compared to methanol and H_2 fuel cells, the H_2O_2 fuel cell has a simple cell structure that does not necessitate the use of membranes to separate the cathode and anode since H_2O_2 can be selectively reduced and oxidized using electrodes in a one-compartment H_2O_2 fuel cell without membranes (Figure 6.2) [Fukuzumi et al., 2012; Fukuzumi & Yamada, 2014; Yamada et al., 2010]. In H_2O_2 fuel cell chemistry, metal ions play a vital role in the electrocatalytic activity of cathode materials. Yamada et al. reported pyrazine-bridged 2D polynuclear cyanide complexes containing Fe^{2+} ions as the cathode of one-compartment H_2O_2 fuel cells, demonstrating the importance of Fe^{2+} ions for high power density.[Yamada et al., 2014] In addition, there is a report of an H_2O_2 fuel cell that uses Fe^{+2} containing $[Fe^{II}(H_2O)_2]_3[Co^{III}(CN)_6]_2$ complex as a cathode and whose OCP and power density have been improved by adding Sc^{3+} ions [Yamada et al., 2015]. Yamada et al. also reviewed the significant role of the presence of N-bound Fe^{2+} ions in improving cathodic activity in a single-compartment H_2O_2 fuel cell.

In our endeavor to find novel properties attributed to formazanate-based metal complexes and the importance of Fe^{+2} in the electrocatalytic activity of cathode materials, herein, we describe

the synthesis and comprehensive (solution and solid-state) characterization of two novel formazan derivatives containing benzothiazole substituents which were further used to synthesize two new electroactive iron(II) formazanate complexes [$Fe^{II}(L2)_2$] (**4**) and [$Fe^{II}(L1)_2$] (**5**). Complexes **4** and **5** were additionally employed as the cathode materials of one-compartment H_2O_2 fuel cells, leading to peak power density (PPD) of 1.88 mW cm^{-2} and 3.01 mW cm^{-2}, respectively. The low cost, tuneability, and ready availability of formazanate ligands make them an attractive platform for developing redox-active systems without being restricted to metal ions as sites of oxidation and reduction, and as a result, it may be more widely applied to other electrocatalytic applications as well.

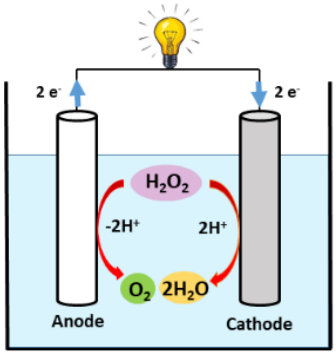


Figure 6.2. Schematic diagram of the one-compartment fuel cell.

6.2 Experimental Section

6.2.1 General Considerations

All of the reagents and chemicals used in the synthesis of formazan ligands, L1H, L2H, and bis(formazanate)iron complexes **4** and **5,** were obtained from commercial sources without being purified further. The synthesis of complexes **4** and **5** was performed in a nitrogen atmosphere. 2-Hydrazinobenzothiazole, 97% and 1-Pyrenecarboxaldehyde, 99%, 2-Amino-5-chlorobenzophenone, 98% were purchased from Sigma-Aldrich. Ferrous chloride and ferrous sulfate heptahydrate were received from Fisher Scientific Company. Hydrochloric acid, 37%, and all the solvents used were purchased from Fisher Scientific Company. In Chapter 2, detailed descriptions of the instruments used for various characterizations are provided.

6.2.2 Synthesis of 1-(benzothiazol-2-yl)-5-phenyl-3-(pyren-1-yl)formazan, L2H

A suspension of 2-hydrazinobenzothiazole (0.330 g, 2.0 mmol, 1.0 eq) in MeOH (25 mL) was treated with glacial acetic acid (0.2 mL), resulting in partial dissolution. After adding 1-pyrenecarboxaldehyde (0.461 g, 2 mmol, 1.0 eq) in one portion, yellow precipitates were formed after 5-10 min. In a separate flask, aniline (0.2 ml, 2.2 mmol, 1.1 eq) was added in a solution of 12 M HCl (0.33 mL, 4 mmol) in H_2O (20 mL) at 0 °C, to which a solution of $NaNO_2$ (0.50 g, 7.3 mmol) in H_2O (5 mL) at 0 °C was added resulting in the formation of the corresponding diazonium salt. The mixture was allowed to stir for another 30 minutes, which was further added to the initial reaction mixture dropwise, resulting in the formation of a dark red solid. Further, the coupling reaction mixture was allowed to stir for another 5 h. The red precipitate was collected by filtration and dried overnight. The crude solid was further purified by column chromatography (dichloromethane, neutral alumina) to afford the red solid. Yield: 528 mg (45%). ^{1}H NMR (500 MHz, $CDCl_3$) δ 8.26 (d, *J* = 7.7 Hz, 2H), 8.22 – 8.15 (m, 3H), 8.08 (dd, *J* = 19.8, 10.2 Hz, 4H), 7.87 (d, *J* = 7.6 Hz, 2H), 7.80 (s, 1H), 7.73 (d, *J* = 8.9 Hz, 2H), 7.45 (s, 2H), 7.24 (d, *J* = 6.5 Hz, 1H), 7.16 (s, 1H). ppm. ^{13}C{^{1}H} NMR (126 MHz, $CDCl_3$): δ 159.04, 152.71, 132.93, 132.72, 131.82, 131.07, 130.81, 129.98, 129.50, 129.40, 129.00, 128.82, 128.02, 127.35, 127.13, 126.81, 126.51, 126.31, 126.13, 126.02,

125.18, 124.92, 123.87, 123.55, 123.39, 123.12, 121.34, 120.14 ppm. FT-IR (KBr): 3452 (m), 3041 (m), 2921 (w), 1591(m), 1542 (s), 1446 (m), 1323 (w), 1245 (m), 1137 (m), 1024 (w), 846 (m), 756 (m), 680 (m), 611 (m) cm^{-1}. UV–vis ($CHCl_3$): λ_{max} 340 nm (ε = 14,700 M^{-1} cm^{-1}), 442 nm (ε = 11,550 M^{-1} cm^{-1}). MS (HRMS, positive-ion mode). Exact mass calcd for $[C_{30}H_{19}N_5S+H]^+$: 482.1361. The exact mass found: 482.1441.

6.2.3 Synthesis of $[Fe^{II}(L1)_2]$, 4

The formazan, L2H (96.30 mg, 0.20 mmol) was dissolved in methanol (15 mL) and allowed to stir for 10 min. Then ferrous chloride (12.7 mg, 0.1 mmol) was further added to the above solution and was kept on stirring for 24 hours at room temperature under the nitrogen atmosphere, during which a dark brown precipitate formed. After washing with methanol and hexane, the precipitates were dried in the air. Further, the crude solid was dissolved in an acetonitrile/dichloromethane solution and allowed to evaporate slowly, yielding single crystals suitable for single-crystal XRD. Yield: 75 mg (74%). ^{1}H NMR (400 MHz, $CDCl_3$) δ 8.92 (d, *J* = 8.1 Hz, 2H), 8.54 (d, *J* = 8.0 Hz, 2H), 8.33 – 8.15 (m, 8H), 8.01 (dt, *J* = 30.0, 8.3 Hz, 6H), 7.59 (d, *J* = 8.4 Hz, 3H), 7.42 – 7.28 (m, 7H), 7.02 (dd, *J* = 26.8, 19.6 Hz, 7H) ppm. ^{13}C NMR (126 MHz, $CDCl_3$) δ 176.51, 161.38, 153.75, 147.27, 132.74, 132.48, 131.30, 130.95, 130.60, 129.25, 128.91, 128.80, 128.67, 128.54, 127.97, 127.51, 127.47, 126.10, 125.68, 125.62, 125.56, 125.51, 124.72, 122.95, 122.78, 122.23, 121.84, 116.59. FT-IR (KBr): 3051 (w), 2401(w), 1714 (m), 1593 (w), 1415 (s), 1215 (s), 1189 (s), 1130 (m), 950 (w), 846 (m), 752 (m), 696 (m) cm^{-1}. UV–vis ($CHCl_3$): λ_{max} 344 nm (ε = 13,850 M^{-1} cm^{-1}),542 nm (ε = 6100 M^{-1} cm^{-1}), 692 nm (ε = 4400 M^{-1} cm^{-1}). MS (HRMS, positive-ion mode). Exact mass calcd for $[C_{60}H_{36}FeN_{10}S_2+H]^+$: 1017.1915 Exact mass found: 1017.2043. Anal. Calcd. (%) for $C_{60}H_{36}FeN_{10}S_2$: C, 70.86; H, 3.57; N, 13.77. Found: C, 70.62; H, 3.84; N, 13.26.

6.2.4 Synthesis of $[Fe^{II}(L2)_2]$, 5.

The formazan, L1H (99.20 mg, 0.20 mmol), was dissolved in methanol (15 mL) and allowed to stir for 10 min. Then ferrous sulfate heptahydrate (27.8 mg, 0.1 mmol) was added to the above solution and was kept on stirring for 24 hours at room temperature under the nitrogen atmosphere, during which a dark purple precipitate formed. After washing with methanol and hexane, the precipitate was dried in the air. Further, the crude solid was recrystallized by the vapor diffusion of hexane into a saturated dichloromethane/methanol solution, yielding single crystals suitable for single-crystal XRD. Yield: 70 mg (67%). ^{1}H NMR (400 MHz, $CDCl_3$) δ 8.21 (dd, *J* = 6.4, 2.9 Hz, 4H), 7.51 – 7.42 (m, 6H), 7.41 – 7.29 (m, 8H), 7.10 (t, *J* = 7.6 Hz, 6H), 7.02 – 6.87 (m, 8H), 6.77 (d, *J* = 8.7 Hz, 2H) ppm. ^{13}C NMR (126 MHz, $CDCl_3$) δ 192.93, 175.75, 160.27, 150.45, 146.77, 136.30, 135.88, 133.24, 132.90, 132.83, 130.93, 129.66, 129.61, 129.08, 128.73, 128.42, 128.08, 127.49, 125.73, 122.40, 121.71, 116.66 ppm. FT-IR (KBr): 3062 (w), 2403 (m), 2289 (w), 1708 (m), 1662 (m), 1544 (w), 1407 (m), 1249 (m), 1218 (s), 1168 (s), 1114 (m), 945 (m), 723 (m), 690 (m), 507 (w) cm^{-1}. UV–vis ($CHCl_3$): λ_{max} 336 nm (ε = 13514 M^{-1} cm^{-1}), 546 nm(ε = 11500 M^{-1} cm^{-1}), 733 nm (ε = 6100 M^{-1} cm^{-1}). Exact mass calcd for $[C_{54}H_{34}Cl_2FeN_{10}O_2S_2+H]^+$: 1045.1034 Exact mass found: 1045.2566. Anal. Calcd. (%) for $C_{54}H_{34}Cl_2FeN_{10}O_2S_2$: C, 62.02; H, 3.28; N, 13.39. Found: C, 62.169; H, 3.049; N, 13.330.

6.2.5 Electrochemical Reduction of Hydrogen Peroxide

A glassy carbon electrode was modified with a small amount (10.0 µL) of a solution prepared by dissolving 5mg of iron complexes **4** and **5** in 1 mL DMF. In order to protect the film on the glassy carbon, 5uL of nafion solution was added, and then the film was dried at 70 °C. These modified glassy carbon electrodes were used as the working electrodes. For the reference electrode, an Ag/AgCl electrode was used, whereas for the counter electrode, a Pt electrode. At ambient temperature, measurements were conducted in 0.1 M HCl containing 100 mM H_2O_2 at a scan rate of 10 mV s^{-1}. Using the CHI-6154E Electrochemical Analyzer, the electrochemical behavior of H_2O_2 at an iron(II)-modified electrode was investigated.

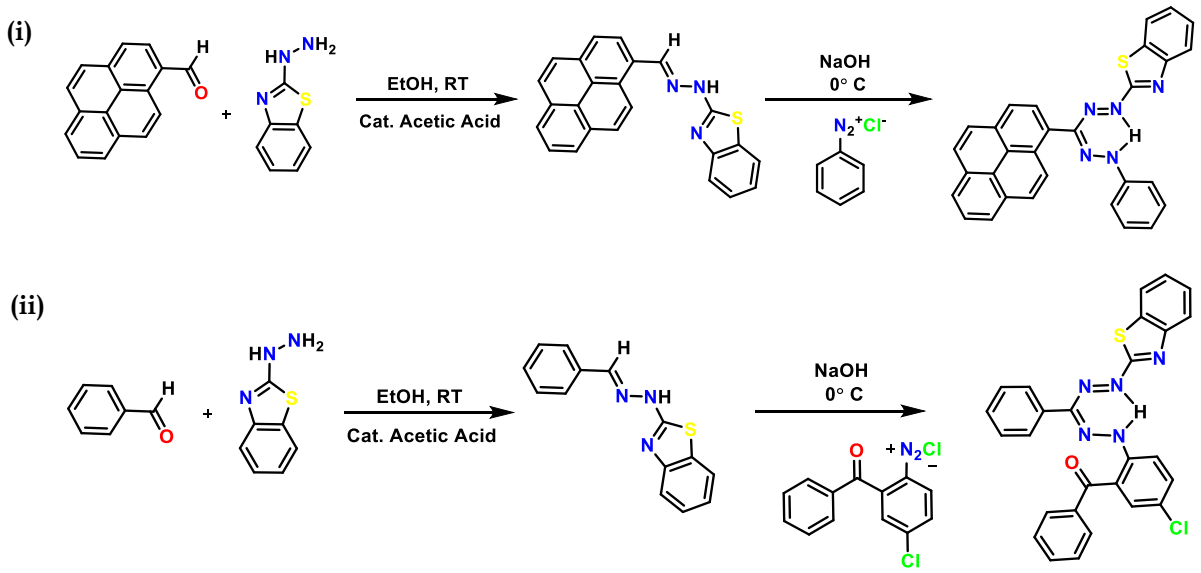
6.2.6 Evaluation of the Performance of a H_2O_2 Fuel Cell

A drop-casting technique was used to mount the iron complexes **4** and **5** onto a glassy carbon electrode. A 5 µL of nafion solution was used to protect the film of the iron complexes on the glassy carbon electrode. An aqueous solution of 0.1 M HCl that contained H_2O_2 (0.50 M) was placed in a one-compartment electrochemical cell. The carbon mixed sample was prepared by pulverizing iron complexes with 10% (wt/wt) carbon black using NMP (N-methyl pyrrolidine) in a mortar and pestle. The finely grounded sample (10.0 µL) was then coated on a GC electrode, followed by 5 µL nafion. A Ni foam and the modified glassy carbon electrodes were immersed in the 0.1 M HCl solution containing H_2O_2 (0.50M). Cell performance was evaluated by using a CHI-6154E electrochemical analyzer at 25 °C.

6.3 Results and Discussion

6.3.1 Synthesis and Characterization of Hetarylformazans

Formazan ligand L2H was synthesized by condensing 2-hydrazinobenzothiazole with 1-pyrene carboxaldehyde, resulting in the formation of the desired hydrazone. Coupling of in situ generated hydrazone with appropriate aryl diazonium chloride salt of aniline in the presence of NaOH produced a reaction mixture from which it was possible to obtain the desired formazan in moderate yield (Scheme 6.1). Formazan ligand L1H was synthesized by following the reported procedure provided in Chapter 5 and was fully characterized. This modular synthetic procedure allows the preamble of several different substitution patterns comprising various asymmetric derivatives. Formazan derivative L2H exhibits straightforward ^{1}H and ^{13}C NMR spectroscopic features, revealing diagnostic formazan NH shifts in the ^{1}H NMR spectra at 10.81 ppm and consistent with equivalent aromatic groups in both ^{1}H and ^{13}C NMR spectra (Figure 6.3). Further characterizations of the ligand were carried out using UV-Vis, FT-IR spectroscopy, and mass spectrometry (Figure 6.3). The identification of N–H weak bands in the FTIR spectral data at the wavelength of 3452 cm^{-1} for L2H suggests the presence of existing intramolecular hydrogen bonding within the formazan molecules (Figure 6.3(b)). The presence of strong bands at 1446 cm^{-1} for L2H indicates the presence of the –N=N– group. Additionally, the distinct C=N stretching bands in formazans are observed at 1596 cm^{-1} for L2H, which aligns well with the published FTIR values [Turkoglu & Berber, 2016]. HRMS studies of L2H showed the presence of molecular ion peaks at m/z 482.1441 (Figure 6.3(a)).



Scheme 6.1. Synthesis of benzothiazole-substituted formazans, (i) L2H (ii) L1H.

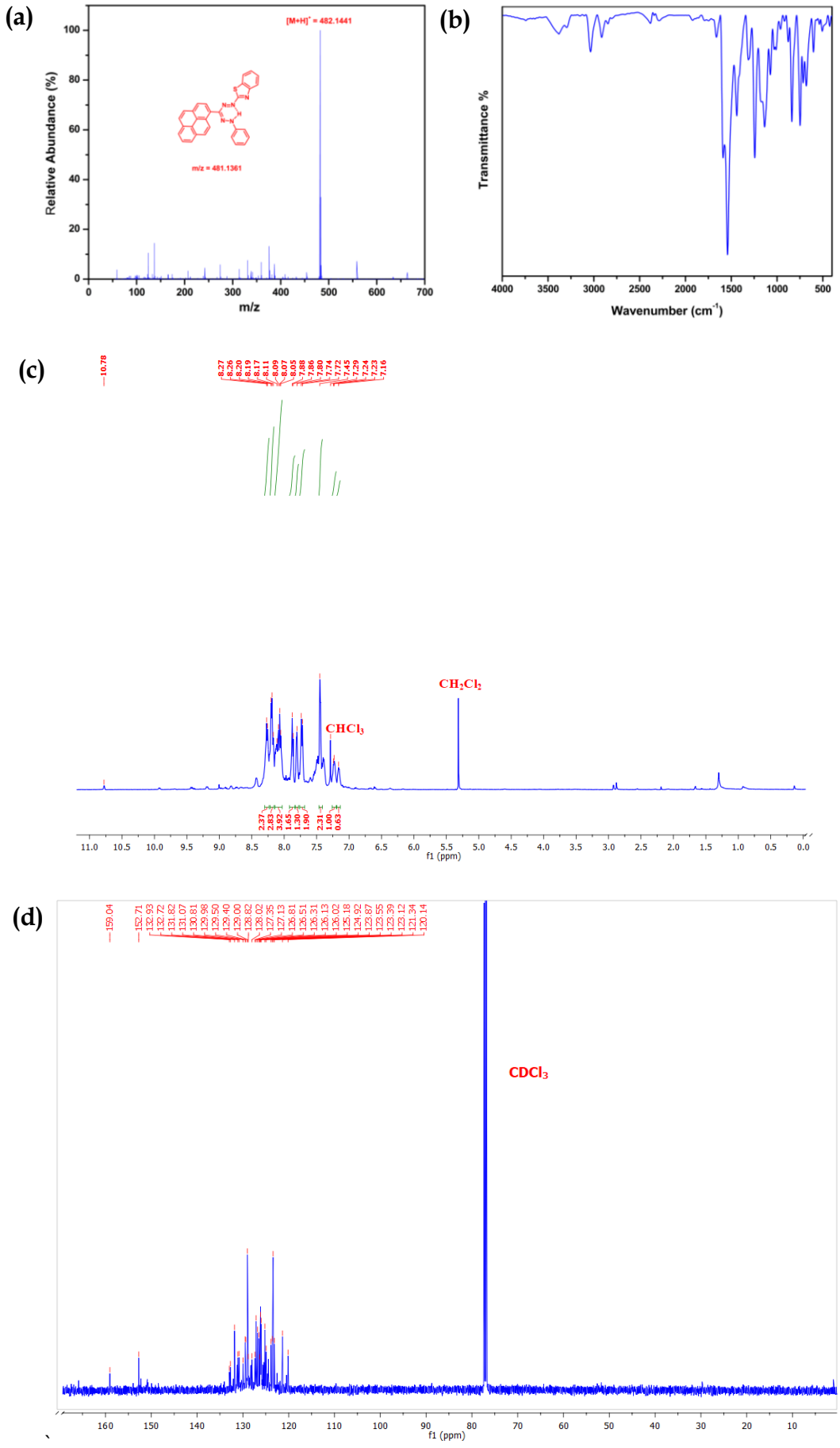
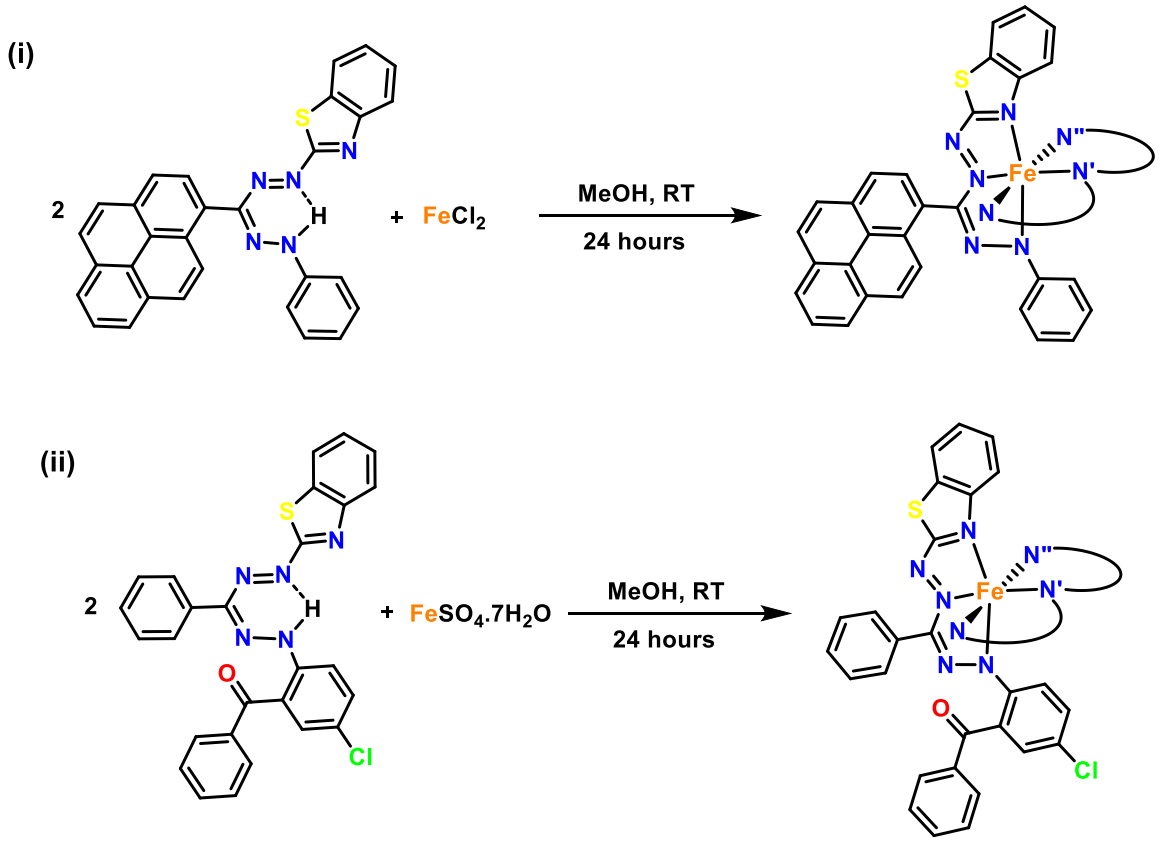


Figure 6.3. (a) HRMS analysis for L2H: Anal. Calcd. for $[M+H]^+$ peak, m/z = 482.1361. Found $[M+H]^+$ peak, m/z = 482.1441. (b) IR spectrum of L2H (c) ^1H NMR of L2H in $CDCl_3$ (d) $^{13}C\{^1H\}$ NMR of L2H in $CDCl_3$.

6.3.2 Synthesis and Characterization of Bis(formazanate)iron Complexes, 4 and 5

The reactions of corresponding hetarylformazans, L2H, and L1H with iron(II) chloride and iron(II) sulfate heptahydrate in methanol at room temperature for 24 h, produce discrete bis(formazanate)iron complexes **4** and **5,** respectively (Scheme 6.2). The molecular structure of both the iron(II) complexes was confirmed using the single-crystal XRD technique. Complexes **4** and **5** were isolated in purified yields of 74% and 67%, respectively, and characterized using ^{1}H, $^{13}C\{^{1}H\}$, UV−vis absorption and FT-IR spectroscopy, cyclic voltammetry, thermogravimetric analysis, elemental analysis, XPS and mass spectrometry. The formation of the iron(II) formazanates, **4** and **5** was evinced by an immediate color change from red to dark brown and dark purple, respectively. The reaction in both cases involves the loss of NH protons from the ligand and subsequent coordination of the Fe(II) center by two deprotonated ligand molecules. The lack of N–H weak bands in the FTIR spectrum data at the wavelengths of 3452 cm^{-1} for **4** and 3444 cm^{-1} for **5** indicates that the ligands coordinate with the metal in their anionic form (Figure 6.4). HRMS studies of **4** and **5** showed the presence of the respective molecular ion peaks at m/z 1017.2043 and 1045.2566 (Figure 6.4). Thermogravimetric analysis (TGA) has shown that complex **4** is stable up to a temperature of 294 °C, while complex **5** remains stable up to 260 °C (Figure 6.6). The XPS method demonstrates that the Fe-centers in both complexes **4** and **5** are in the +2 oxidation state. The binding energies (BEs) for the Fe $2p_{3/2}$ and Fe $2p_{1/2}$ spin components are found to be at 719.6 and 706.8 eV, respectively, from the Fe 2p XPS spectra of the complex **4** (Figure 6.4). Meanwhile, for complex **5**, binding energies for Fe $2p_{3/2}$ and Fe $2p_{1/2}$ are found at 719.85 and 707.1 eV, respectively (Figure 6.4). These values are characteristic of Fe(II) centers present in both complexes.



Scheme 6.2 Synthesis of bis(formazanate)iron complexes, (i) **4** (ii) **5** (only one ligand shown in full, other abbreviated (N, N', N") for clarity).

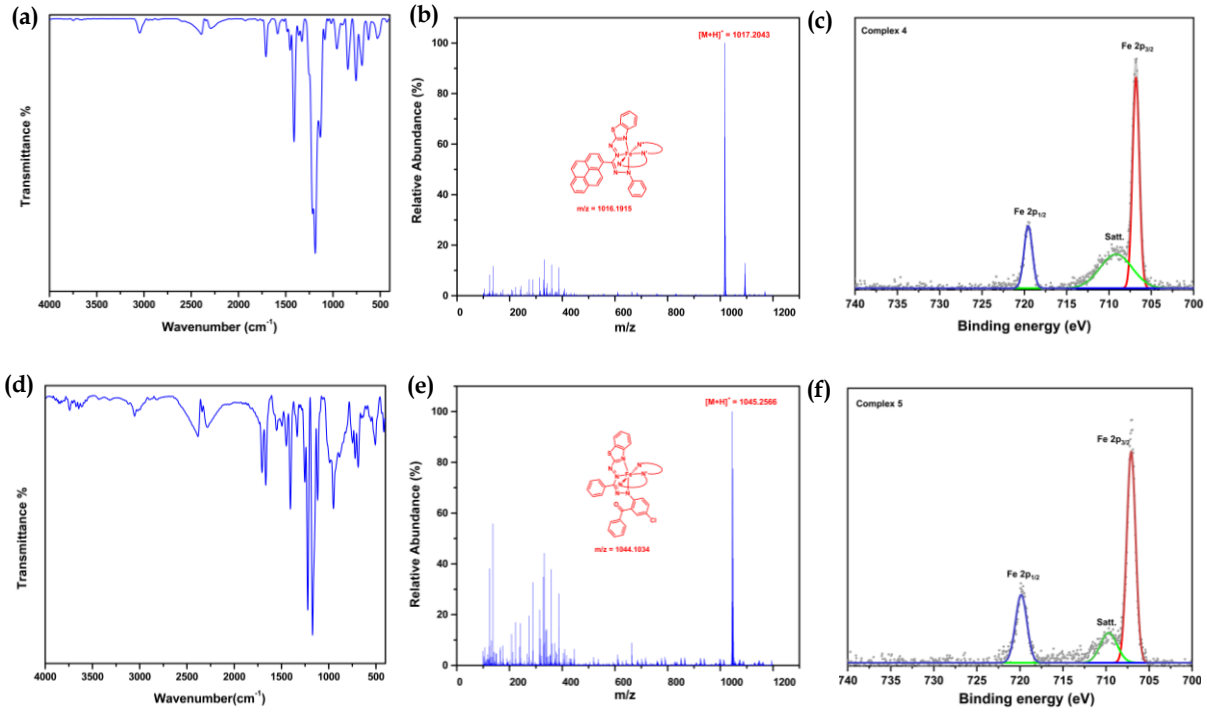
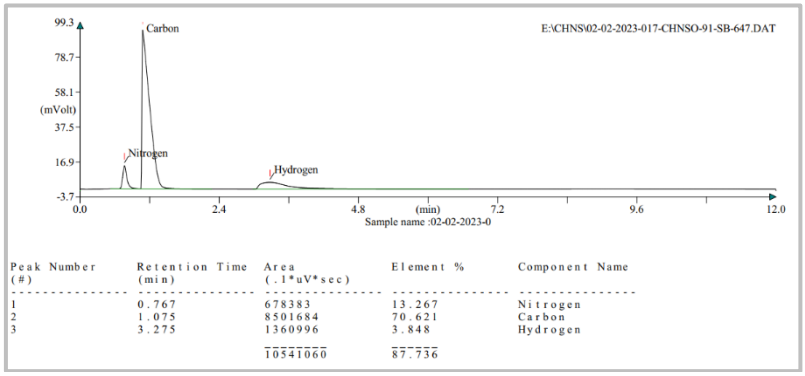


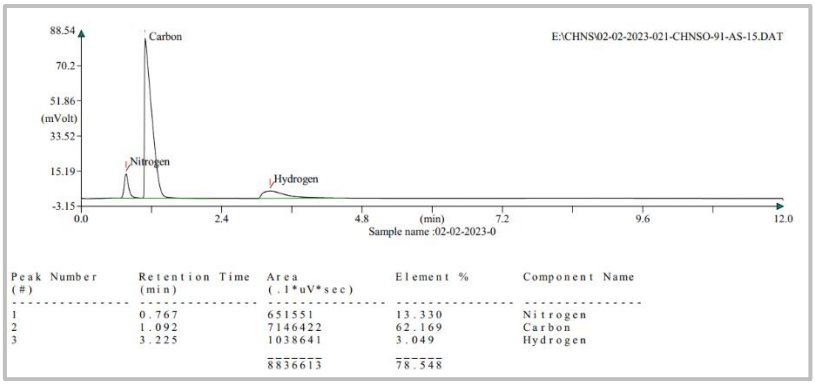
Figure 6.4 (a) IR spectrum of complex **4** **(b)** HRMS analysis for **4**: Anal. Calcd. for $[M+H]^+$ peak, m/z =1017.1915. Found $[M+H]^+$ peak, m/z = 1017.2043. (c) XPS-analysis for the Fe 2p binding energies of complex **4** (d) IR spectrum of complex **5** (e) HRMS analysis for **5**: Anal. Calcd. for $[M+H]^+$ peak, m/z =1045.1034. Found $[M+H]^+$ peak, m/z = 1045.2566. (f) XPS-analysis for the Fe 2p binding energies of complex **5**.

(a)



Peak Number (#)	Retention Time (min)	Area (.1*uV*sec)	Element %	Component Name
1	0.767	678383	13.267	Nitrogen
2	1.075	8501684	70.621	Carbon
3	3.275	1360996	3.848	Hydrogen
		10541060	87.736	

(b)



Peak Number (#)	Retention Time (min)	Area (.1*uV*sec)	Element %	Component Name
1	0.767	651551	13.330	Nitrogen
2	1.092	7146422	62.169	Carbon
3	3.225	1038641	3.049	Hydrogen
		8836613	78.548	

Figure 6.5 (a) Elemental analysis of **4.** Anal. Calcd. (%) for $C_{60}H_{36}FeN_{10}S_2$: C, 70.86; H, 3.57; N, 13.77. Found: C, 70.62; H, 3.84; N, 13.26. (b) Elemental analysis of **5.** Anal. Calcd. (%) for $C_{54}H_{34}Cl_2FeN_{10}O_2S_2$: C, 62.02; H, 3.28; N, 13.39. Found: C, 62.169; H, 3.049; N, 13.330.

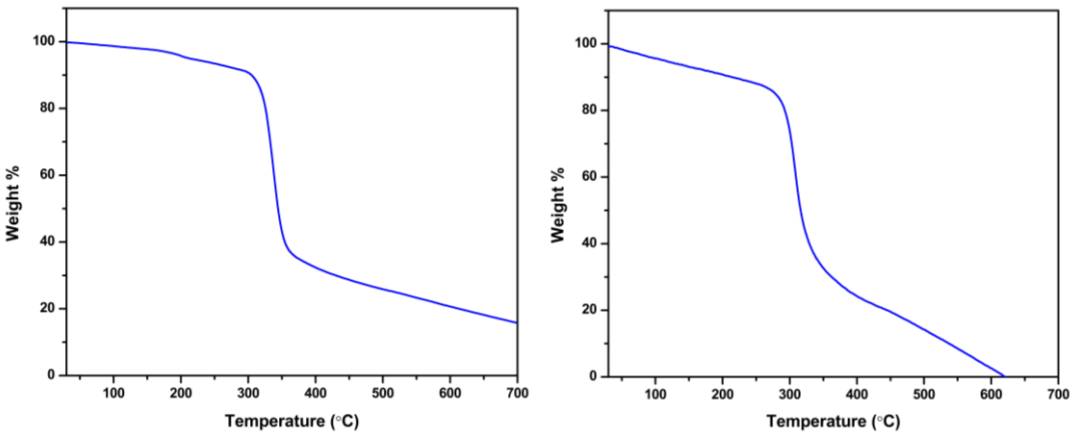


Figure 6.6. Thermogravimetric analysis of (left) complex **4**, (right) complex **5**.

6.3.3 X-Ray Crystallography

The dark brown single crystals of **4** were prepared using a slow evaporation method, whereas the dark purple single crystals of **5** were grown using the vapour diffusion method. Single-crystal X-ray diffraction (SCXRD) analyses revealed that both of these compounds possess the same coordination structure that the Fe^{II} metal center is chelated by six N atoms from the benzothiazole-substituted formazan ligands to form a pseudo octahedral structure with the FeN6 coordination sphere involving the N1 and N3 nitrogen atoms of the formazanate scaffold and the N5 heterocyclic nitrogen of each of the two formazan molecules resulting in four fused CN3Fe five-membered rings (Figure 6.7). Crystal **4** belongs to a triclinic P-1 space group with the lattice filled with CH_2Cl_2 molecules with two molecules per unit cell, whereas the crystal solvent was not found in the compound **5,** and it crystallized in monoclinic $P2_1/n$ space group with four molecules per unit cell. The crystal structure refinement parameters of both complexes **4** and **5** are listed in Table 6.1. The single-crystal structural analyses revealed that the Fe–N bond lengths of the coordination octahedron differ in length even though all its vertices are occupied by nitrogen atoms; they can be divided into three groups, each with two bonds. The two shortest Fe–N bond lengths are 1.884 Å each for **4** and 1.887 and 1.895 Å for **5**, formed by the N3 and N8 atoms, which occupy the opposite positions, suggesting that the octahedron is compressed along the N3···N8 axis. The intermediate Fe–N bond lengths, for **4**, 1.933, and 1.942 Å, are formed with the N6 and N1 atoms, whereas for **5**, 1.963, and 1.977 Å, are formed with the N1 and N6 atoms, respectively. Fe atoms are most distant from N5 and N10 atoms, having bond distances of 1.996 and 1.991 Å, respectively, in **4**, while the bond distances are 2.002 and 2.007 Å in **5**. The Fe−N bonds in these complexes are comparable to the bond lengths in reported octahedral Fe(II) complexes [Brown et al., 1998; Gorbatenko et al., 2008; Müller et al., 1994]. The selected bond distances and bond angles of these complexes are summarized in Table 6.2. Equivalent intraligand C-N and N-N bond lengths indicate full charge delocalization on the NNCNN ligand backbone in both complexes. In both cases, the formazan ligands occupy planes that are almost perpendicular to each other. For example, in **4**, the N1–Fe01–N5 angle is 156.24° shows deviation of 23.78° from 180° whilst in **5**, N1–Fe1–N5 angle is 157.11° indicates the deviation of 22.89° from 180°. Because of the bulky substituents, these distortions arise from the ideal octahedral coordination geometry. The angle between the formazanate coordination planes for **4** is 83.271°, whereas for **5,** it is increased to 86.661°.

C-H--π and π--π interactions coalesce to form a three-dimensional network in the molecular packing of complex **4** (Figure 6.8). Complex **4** contains two molecules per unit cell, as depicted in Figure 6.8(a), where the adjacent Fe--Fe distance is 9.635 Å and C-H--π interactions exist between them. In addition, the molecule interacts with its neighbors via interactions between two pyrene groups separated by centroid distances of 3.574 Å [Figure 6.8(b)]. Four molecules constitute the unit cell in complex **5**, where the separations between the iron atoms are

8.430 and 10.931 Å, and they interact with each other via C-H--π and C-H--O interactions [Figure 6.9**(a)**]. Additionally, CH--π and CH--Cl interactions result in the formation of supramolecular assembly in complex **5** [Figure 6.9(b)].

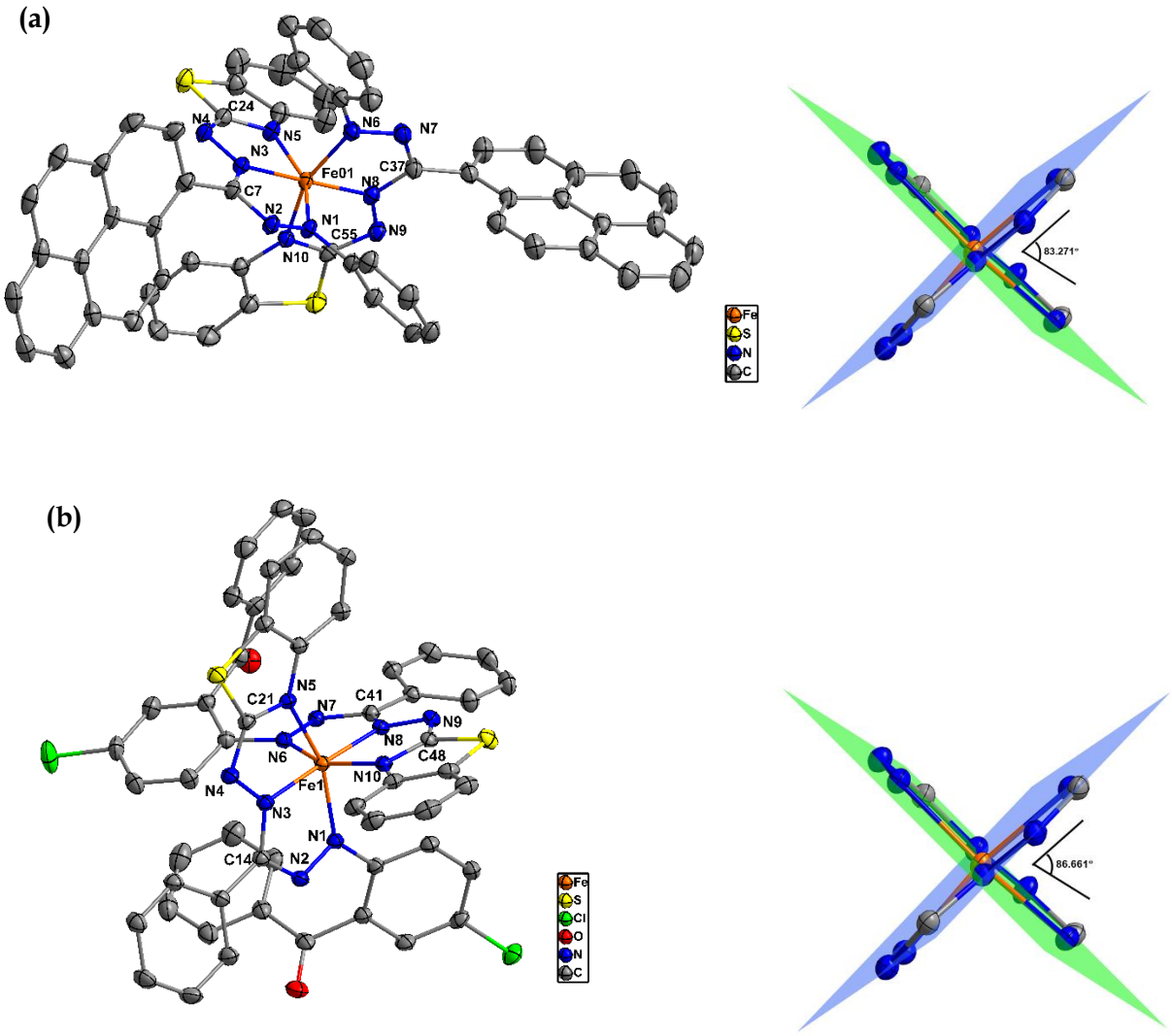


Figure 6.7. (a) (Left) Molecular structure of **4** showing 50% probability ellipsoids. (Right) The $Fe(NNCNNCN)_2$ core of the structure with the N–Fe–N planes and the dihedral angle. (b) (Left) Molecular structure of **5** showing 50% probability ellipsoids. (Right) The $Fe(NNCNNCN)_2$ core of the structure with the N–Fe–N planes and the dihedral angle.

Table 6.1. Crystal data and structure refinement for **4** and **5** (CCDC 2376420-2376421) **.**

Identification code	4	5
Empirical formula	$C_{61}H_{38}Cl_2FeN_{10}S_2$	$C_{54}H_{34}Cl_2FeN_{10}O_2S_2$
Formula weight	1101.88	1045.78
Temperature/K	98(2)	98(2)
Crystal system	Triclinic	monoclinic
Space group	P-1	$P2_1/n$
a (Å)	12.155(3)	11.2395(4)
b (Å)	14.292(3)	31.2736(10)

c (Å)	16.758(4)	13.8511(5)
α (°)	114.981(5)	90
β (°)	97.046(6)	111.7710(10)
γ (°)	101.320(6)	90
Volume (Å^3)	2517.5(9)	4521.4(3)
Z	2	4
ρ_{calc}, g.cm^{-3}	1.454	1.536
μ (mm^{-1})	0.543	0.603
F(000)	1132.0	2144.0
Radiation	MoK$_\alpha$ (λ = 0.71073)	MoK$_\alpha$ (λ = 0.71073)
2Θ range for data collection (°)	5.3 to 56.746	4.782 to 56.72
Index ranges	-16 ≤ h ≤ 16, -19 ≤ k ≤ 19, -22 ≤ l ≤ 22	-14 ≤ h ≤ 15, -41 ≤ k ≤ 41, -18 ≤ l ≤ 18
Reflections collected	39556	73504
Independent reflections	12571 [R_{int} = 0.0454, R_{sigma} = 0.0487]	11259 [R_{int} = 0.0576, R_{sigma} = 0.0383]
Data/restraints/parameters	12571/0/685	11259/0/640
Goodness-of-fit on F^2	1.037	1.040
Final R indexes [I>=2σ (I)]	R_1 = 0.0724, wR_2 = 0.2009	R_1 = 0.0401, wR_2 = 0.0864
Final R indexes [all data]	R_1 = 0.0923, wR_2 = 0.2203	R_1 = 0.0566, wR_2 = 0.0964
Largest diff. peak/hole / (e Å^{-3})	1.17/-2.16	0.44/-0.52

Table 6.2. Selected Bond Distances (Å) and Selected Bond Angles (deg) for **4** and **5**.

	4		**5**
N1-N2	1.303(48)	N1-N2	1.304(23)
N2-C7	1.360(36)	N2-C14	1.356(23)
C7-N3	1.334(50)	C14-N3	1.347(22)
N3-N4	1.351(37)	N3-N4	1.348(20)
N4-C24	1.346(57)	N4-C21	1.346(23)
C24-N5	1.340(53)	C21-N5	1.331(25)
Fe01-N1	1.942(31)	Fe1-N1	1.963(14)
Fe01-N3	1.884(32)	Fe1-N3	1.895(17)
Fe01-N5	1.996(29)	Fe1-N5	2.002(14)
N1–Fe01–N3	78.26(124)	N1–Fe1–N3	78.31(71)
N3–Fe01–N5	78.72(120)	N3–Fe1–N5	78.97(67)
N6–Fe01–N8	78.64(118)	N6–Fe1–N8	78.11(69)
N8–Fe01–N10	78.38(124)	N8–Fe1–N10	78.98(66)
N1–Fe01–N5	156.24(116)	N1–Fe1–N5	157.11(69)
N3–Fe01–N8	177.73(134)	N3–Fe1–N8	177.55(74)
N6–Fe01–N10	157.01(112)	N6–Fe1–N10	156.23(67)

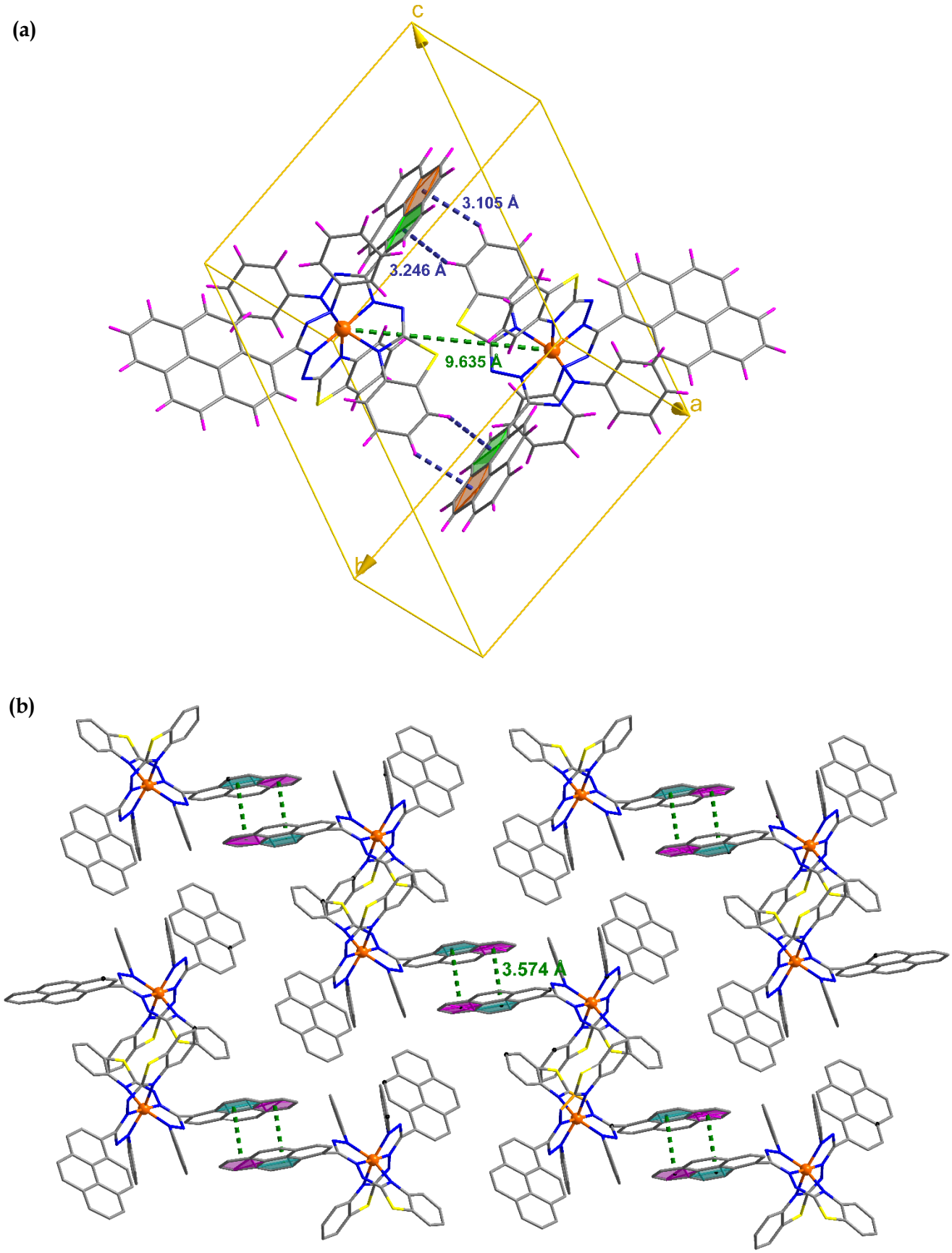


Figure 6.8. (a) Unit cell of complex **4** showing the C—H··· π interactions. (b) Crystal packing mode for complex **4** displaying π···π interactions.

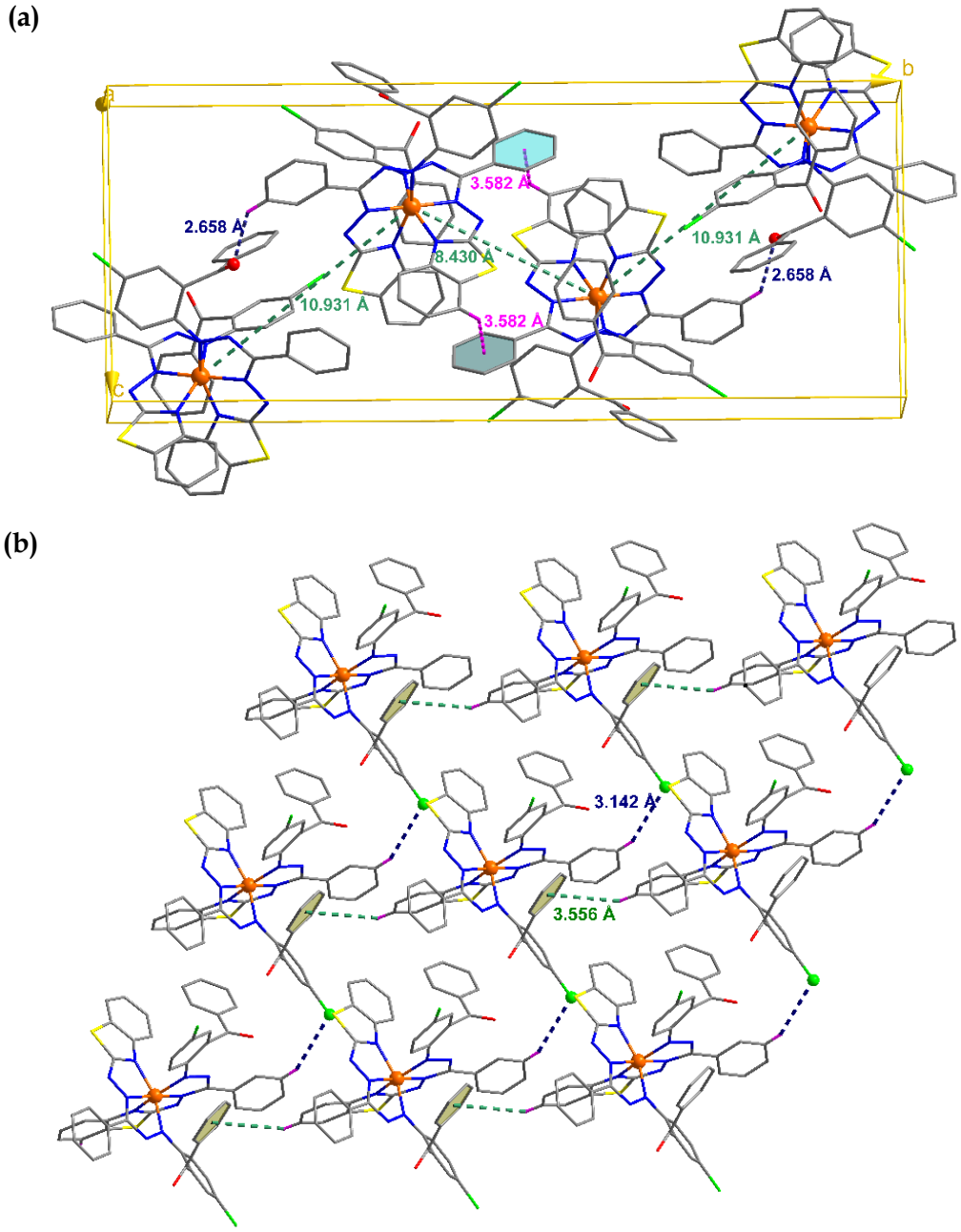


Figure 6.9. (a) Unit cell of complex **5** showing the C—H··· O and C—H··· π interactions. (b) Crystal packing mode for complex **5** displaying C—H···Cl and C—H··· π interactions.

6.3.4 Electronic Spectra

The optical properties of the free ligands and the Fe(II) complexes were obtained by UV−vis absorption spectroscopy of the complexes in chloroform solution in the range of 200-800 nm (Figure 6.10). It is found that the free ligands exhibit a broad, intense band in the 400-550 nm region corresponding to a π-π^* transition of the conjugated system in the formazan NNCNN backbone. In the case of **4**, complexation with Fe(II) gives shifts to longer wavelengths from 440 nm to 546 nm, and for complex **5**, this shift is from 508 nm to 543 nm, consistent with a decrease in π-π^* energy due to interaction with the metal d orbitals. A second intense band, centered at 692 nm and 729 nm for complex **4** and complex **5,** respectively, is tentatively assigned to a metal-to-ligand charge transfer (MLCT) transition. These bands are observed in the corresponding reported Fe(II) bis-formazanate octahedral complexes [Brown et al., 1998; Müller et al., 1994]. In particular, it is interesting that the Fe center electronically combines the two perpendicular electron systems of the rings.

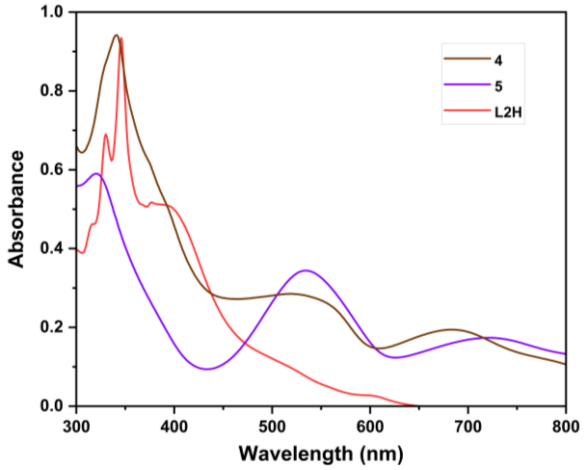


Figure 6.10. Absorption spectra for L2H, **4,** and **5** in $CHCl_3$.

6.3.5 Electrocatalytic Reduction of H_2O_2

Cyclic voltammograms of 0.1 M H_2O_2 in an acetate buffer (pH 3) solution were performed to determine if electrocatalytic reduction of H_2O_2 with a glassy carbon electrode (GC) modified with the iron(II)-complexes **4** and **5** was feasible. The experimental section contains a description of the electrode preparation. In addition, a CV (black) of iron complexes **4** and **5** in an acetate buffer solution without H_2O_2 is included as a reference, as shown in Figure 6.11. A quasi-reversible redox couple was observed for **4** as well as **5** when H_2O_2 was absent, which is assigned to Fe^{2+}/Fe^{3+}. Catalytic currents for H_2O_2 reduction are absent in the cathodic sweep when H_2O_2 is not present, whereas, in the presence of H_2O_2, complexes **4** and **5** showed significant catalytic currents of 250 µA and 275 µA respectively, for H_2O_2 reduction in acetate buffer (pH =3) at onset potential of 0.35 V and 0.45 V (vs. Ag/ AgCl, 3.0 M KCl) respectively which depicts that complexes **4** and **5** exhibit electrocatalytic properties. At the same time, the cyclic voltammograms of 0.1 M H_2O_2 in acidic electrolytes such as 0.1 M HCl, 0.1 M H_2SO_4, and 0.1 M $HClO_4$ under identical conditions, were conducted as the reduction of H_2O_2 is contingent upon the active concentration of H^+ ions, which have shown a significant increase in the current for **4** and **5** respectively (Figure 6.20). For both complexes, it can be observed that the value of cathodic current increases to more negative values in the case of 0.1 M HCl electrolyte than the 0.1 M H_2SO_4 and 0.1 M $HClO_4$, signifying the improvement in electrochemical H_2O_2 reduction in HCl. A parallel set of experiments was conducted on a bare GC electrode under identical conditions. However, no catalytic performance was observed in relation to H_2O_2 reduction.

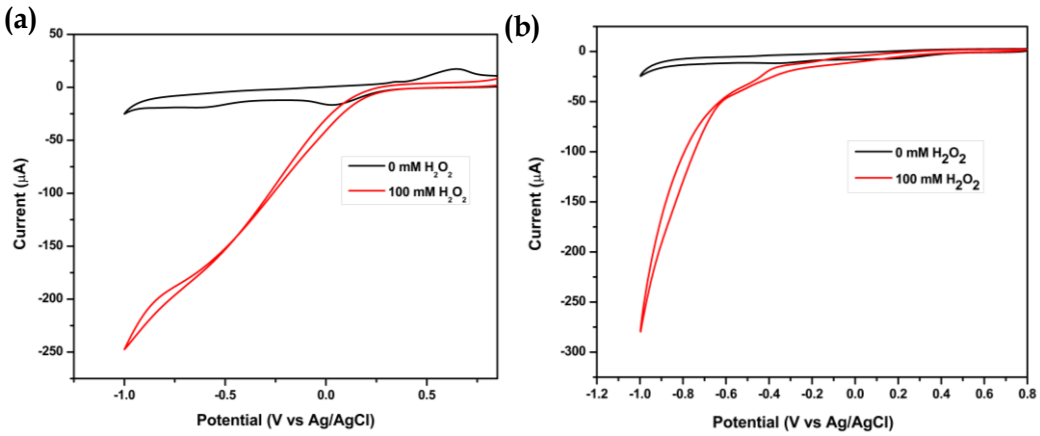
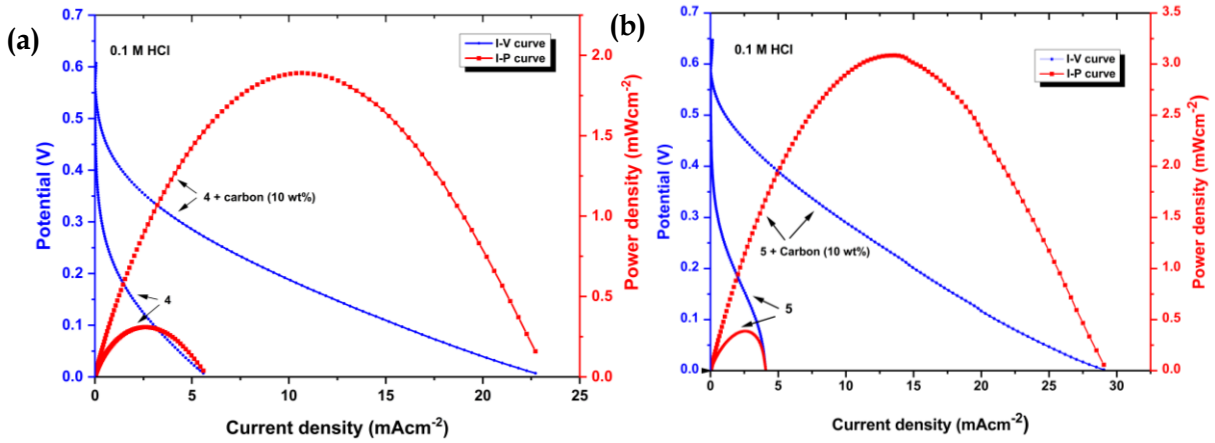


Figure 6.11. Cyclic voltammograms of H_2O_2 in acetate buffer (pH = 3) using GC electrode modified with (a) **4** and (b) **5** as working electrode. Ag/AgCl as a reference and Pt-wire as counter electrode at a scan rate of 10 mV s^{-1}.

6.3.6 Performance of the One-compartment H_2O_2 Fuel Cell

An aqueous solution (0.1 M HCl) containing 0.50 M H_2O_2 was used to evaluate one-compartment H_2O_2 fuel cell performance using a nickel foam anode and a glassy carbon cathode modified with complexes **4** and **5** using a drop-casting method. An electrode of interest should have a lower onset potential for H_2O_2 oxidation than the onset potential for H_2O_2 reduction over GC modified with **4** and **5**. As a case study, H_2O_2 oxidation on a nickel electrode (Ni) varies from -0.09 V to 0.05 V at various pH values [Mousavi Shaegh et al., 2012b; Yamazaki et al., 2008], which is much lower than the onset potential of H_2O_2 reduction with an electrode modified with iron(II) complexes **4** and **5**. Thus, in order to implement the fuel cell, Ni foam was selected as the anode. This suggests that Ni foam as an anode and GC modified with iron(II) complexes **4** and **5** as a cathode are suitable for H_2O_2 fuel cells. An aqueous solution of 0.1 M HCl is the most frequently used electrolyte for this form of one-compartment fuel cell. For complex **4**, the H_2O_2 fuel cell operating in 0.1 M HCl electrolyte found an open-circuit potential value of 0.626 V and produced a maximum power density of 0.327 mWcm$^{-2,}$ as shown in Figure 6.12a. Further, the conductivity was increased by mixing 10 wt % of carbon in **4** to achieve better results. As a consequence, the OCP value increased to 0.67 V, and the power density reached 1.88 mW cm^{-2} for **4**, almost four-fold higher than before (Figure 6.12a). The power output was not further improved when the percentage of carbon loading was increased. Whereas in the case of complex **5**, with 0.1 M HCl as the electrolyte, the addition of 0.5 M H_2O_2 resulted in an OCP value of 0.648 V, and the power density achieved was 0.387 mW cm^{-2}; these values were further improved to 0.69 V and 3.08 mW cm^{-2}, respectively, by mixing 10 wt % of carbon in **5** (Figure 6.12b). Similarly, in this case of **5**, the increase in carbon % did not lead to any additional improvement in power density. Additionally, the fuel cell performance of these complexes was evaluated in electrolytes with concentrations of 0.1 M H_2SO_4 and 0.1 M $HClO_4$ (See 6.5 Appendices). These fuel cells of both the complexes yielded low OCP, which in turn led to a very low PPD.

The OCP values for the **4** and **5** were steadier than those seen in studies without carbon after an examination of 10 consecutive experiments with 10% carbon (Figure 6.12c and 6.12c). UV-vis spectroscopy was employed to verify the stability of complexes **4** and **5** following H_2O_2 fuel cell experiments conducted under optimized conditions (Figure 6.19). Our results have shown improved power density than compounds containing N-bound Fe ions, such as Prussian blue, where iron has a valence between +2 and +3, attained a power density of 1.55 mW cm^{-2} and with Fe_3 [{$Co^{III}(CN)_6$}$_2$] that contains N-bound Fe^{+2} ions, power density of 1.2 mW cm^{-2} was achieved [Yamada et al., 2013, n.d.; Mousavi Shaegh et al., 2012b]. It is evident from these reports that Fe^{2+} ions bound to N in the cathode contribute significantly to the high performance of one-compartment H_2O_2 fuel cells.



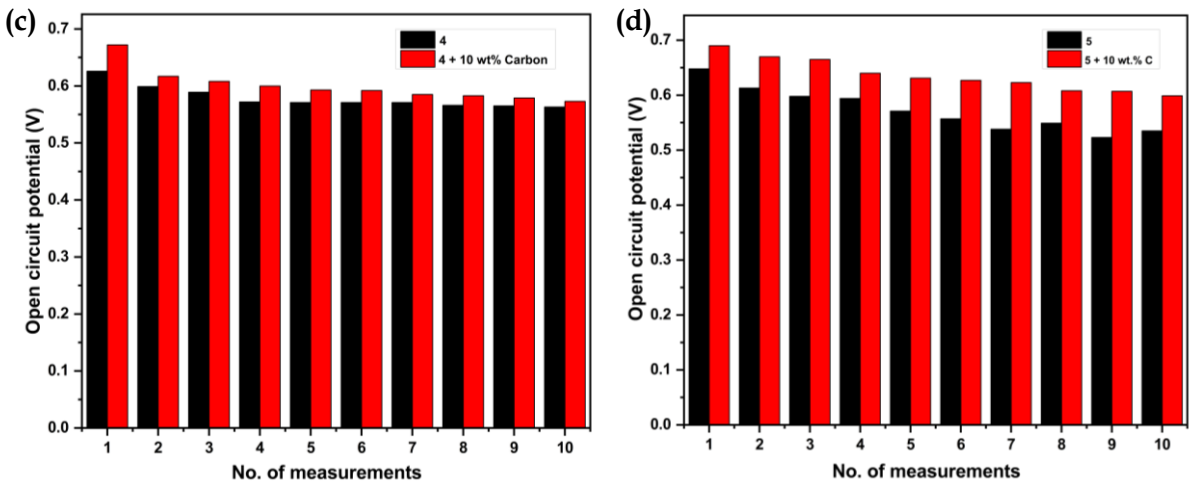


Figure 6.12. Performance test of the single compartment H_2O_2 fuel cell showing I–V (blue) and I–P (red) curves using GC electrode modified with (a) **4** as cathode and (b) **5** as cathode and Ni foam as an anode in 0.1 M HCl containing 0.5 M H_2O_2 at a scan rate 10 mV s^{-1}. The current density is normalized to the geometrical surface area of the GC electrode (0.07 cm^{-2}). The change in open-circuit potential on repetitive measurements for (c) **4** and (d) for **5**.

6.3.7 Cyclic Voltammetry (CV)

In order to understand the electron transfer process within **4** and **5**, we conducted cyclic voltammetric experiments. Formazanate ligands have been shown to be reversibly reduced to their radical anion and diradical dianion in previous literature. As shown in Figure 6.23, in cyclic voltammograms of L2H, three ligand-based quasi-reversible reduction peaks were observed during the cathodic sweep at $E_1^{1/2}$ = -1.42 V(ΔE = 70 mV), $E_2^{1/2}$ = -1.93 V(ΔE = 80 mV), and $E_3^{1/2}$ = -2.16 V(ΔE = 90 mV), (versus Fc/Fc^+) whereas for L1H, two ligand-based quasi-reversible reduction peaks were observed during the cathodic sweep at $E_1^{1/2}$ = -1.43 V(ΔE = 70 mV), $E_2^{1/2}$ = -1.93 V(ΔE = 120 mV). Recent reports suggest that a single formazanate ligand in (formazanate)BF_2 and (formazanate)$_2$Zn compounds undergo two electron reductions to give L^{3-} type structures [Chang et al., 2015d; Maar et al., 2015b]. In the cyclic voltammograms of **4**, a quasi-reversible reduction was observed during the cathodic sweep at $E_1^{1/2}$ = -1.10 V (ΔE = 70mV), which can be assigned to $Fe^{I/II}$ redox couple [Masood et al., 1991; Rao et al., 1976; Travieso-Puente et al., 2016a; Vinod Kumar Vashistha et al., 2021; Voloshin et al., 2018] as it is absent in cyclic voltammogram of L2H, followed by three ligand based quasi-reversible reductions at $E_2^{1/2}$ = -1.41 V(ΔE = 131 mV), $E_3^{1/2}$ = -1.66 V(ΔE = 60 mV), and $E_4^{1/2}$ = -2.10 V(ΔE = 113 mV), (versus Fc/Fc^+) (Figure 6.13). Whereas in case of **5**, a quasi-reversible reduction was observed during the cathodic sweep at $E_1^{1/2}$ = -0.96 V(ΔE = 69 mV) assigned to $Fe^{I/II}$ redox couple [Travieso-Puente et al., 2016a] followed by two ligand-based quasi-reversible reductions at $E_2^{1/2}$ = -1.42 V(ΔE = 144mV) and $E_3^{1/2}$ = -1.91 V(ΔE = 90mV) (versus Fc/Fc^+) (Figure 6.13). Also, it can be seen that the first reduction peak $E_1^{1/2}$ = -0.96 V(ΔE = 69 mV) observed in the case of complex **5** is not observed in the cyclic voltammogram of L1H.

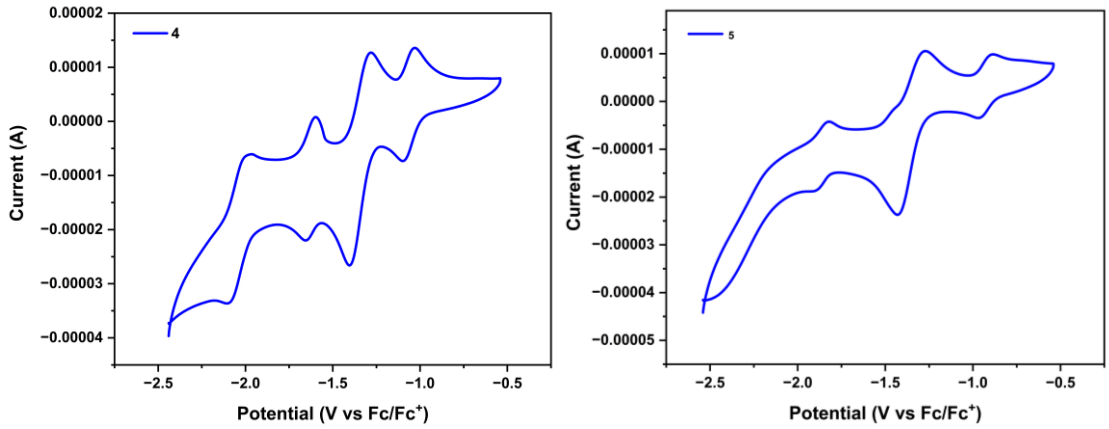


Figure 6.13. Cyclic voltammograms of complex (left) **4** and (right) **5** (1.5 mM solution of iron complexes in DMF; 0.1 M $[Bu_4N][PF_6]$ electrolyte; scan rate = 10 $mV{\cdot}s^{-1}$) obtained using a Pt working electrode, Pt-wire counter electrode, and Ag/AgCl reference electrode.

6.3.8 Proposed Mechanism

Some groups have documented the direct involvement of redox-active ligands in the reduction of H_2O_2 for a molecular cathode constructed from iron-based complexes [Kamboj, Dey, et al., 2023; Pariyar et al., 2015]. The mechanism of the H_2O_2 fuel cell, which utilizes complexes **4** and **5** as the cathode and Ni foam as the anode, may be understood by considering Figure 6.14. As previously stated, the anode facilitates the oxidation of H_2O_2, resulting in the generation of H^+ ions and electrons that migrate toward the cathode. The generated electrons are carried by a high potential between the electrodes, and they then traverse the circuit to reach bis(formazanate) iron(II) complexes, $[Fe^{II}L_2]$ (L= L2, **4**; L1, **5**), and undergo reduction to become $\mathbf{4}^-$ or $\mathbf{5}^-$. The complexes $\mathbf{4}^{-1}$ or $\mathbf{5}^{-1}$ facilitate the transfer of electrons to H_2O_2, and this reaction, in the presence of H^+ ions, leads to the production of H_2O (by route i) and also allows for the regeneration of the catalyst **4** or **5**. The route (i) can thus be seen as a broad approach operating through the Fe(II)/Fe(I) oxidation-reduction process. The reduction described in the pathway (i) involves two separate one-electron reductions, requiring two molecules of $\mathbf{4}^-$ or $\mathbf{5}^-$. Alternatively, we can consider the one-step two-electron reduction of H_2O_2, as demonstrated in route (ii). This approach involves the formation of a two-electron reduced species $\mathbf{4}^{2-}$ or $\mathbf{5}^{2-}$, which is supported by our CV results. This pathway for the reaction can only be effective provided the ligands coordinated to metal have the capacity to store electrons, which is feasible in the case of complexes **4** and **5**. Thus, in the catalytic cycle, complexes **4** and **5**, consisting of formazanate ligands, have the ability to receive two electrons and transform into dianionic species. Further, the complexes $\mathbf{4}^{2-}$ or $\mathbf{5}^{2-}$ can participate in the reduction process of H_2O_2 by transporting two electrons and restoring **4** or **5** by route (ii). Therefore, complexes **4** and **5** have the ability to function through both pathways (i) and (ii) in a cooperative manner, which can significantly impact the performance of the H_2O_2 fuel cell.

After conducting preliminary tests to assess the catalytic activity of complexes **4** and **5**, it was observed that the onset potential for the reduction of H_2O_2 under the same conditions was measured at 0.35 V and 0.45 V, respectively. The enhanced power output in the fuel cell while using complex **5** compared to complex **4** can be attributed to the greater ease of H_2O_2 reduction by complex **5**. Further, the solution-state CV of complex **4** displayed the first Fe-centered reduction event $Fe^{II/I}$ at $E_1{}^{1/2}$ = −1.10 V vs Fc/Fc^+ (ΔE = 70 mV, quasi-reversible), whereas for complex **5**, under identical conditions, the respective reduction events are observed at $E_1{}^{1/2}$ = −0.96 V vs Fc/Fc^+ (ΔE = 69 mV, quasi-reversible). This indicates the facile reduction of the iron center in the case of complex **5**, resulting in an increased power density in the fuel cell based on complex **5**.

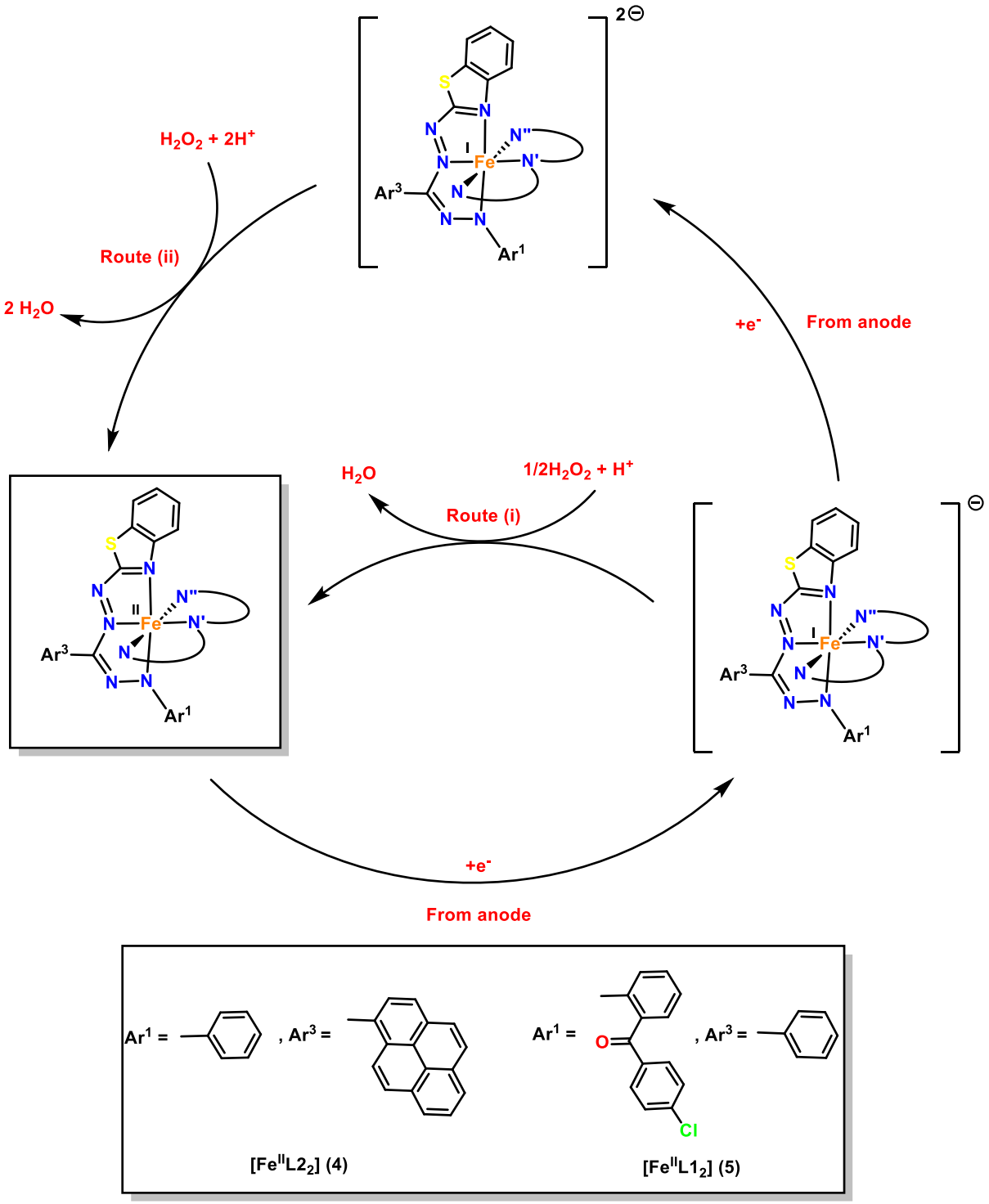


Figure 6.14. Plausible mechanism for the electrocatalytic reduction of H_2O_2 with complexes **4** and **5** employed as the cathode.

6.4 Conclusion

In conclusion, we describe the synthesis of a set of electronically diverse novel formazans L2 and L1, allowing the preparation of two bis(formazanate) iron complexes. The synthesis of the bis(formazanate) iron(II) complexes, [$Fe^{II}L_2$] (L= L2, **4**; L1, **5**), described here were characterized using various analytical techniques, and their molecular structure was confirmed using SC-XRD. Upon structural analysis of the complexes, peculiar five-membered chelate forms were observed, indicating "open form" binding possibilities for formazanate. Complexes based on formazanate ligands provide unique optoelectronic characteristics and diverse electrochemistry that can serve

as a strong foundation for many novel applications. One-compartment H_2O_2 fuel cell working under acidic conditions was constructed by using [$Fe^{II}L_2$] (L= L2, **4**; L1, **5**) as a cathode material and Ni foam as an anode. Complex **4** displayed a peak power density of 1.88 mW cm^{-2}, whereas for complex **5**, the observed power density was 3.08 mW cm^{-2}, higher than the N-bound Fe^{+2} containing compounds. These results illustrate that formazanate-based complexes can be further explored extensively in the design of cathode materials.

6.5 Appendices

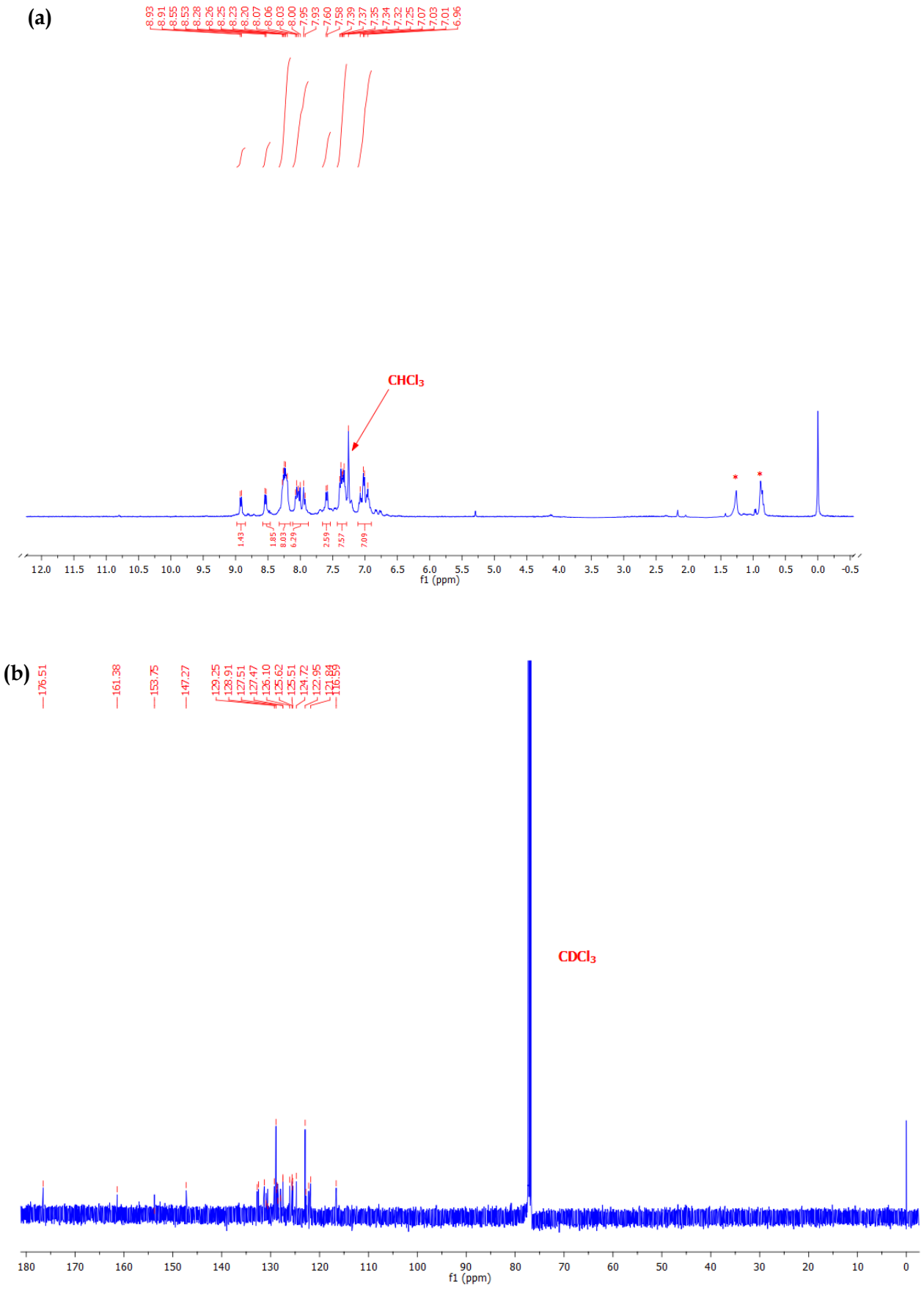


Figure 6.15. (a) ^{1}H NMR (500 MHz, $CDCl_3$) of complex **4**. (b) $^{13}C\{^{1}H\}$ NMR (126 MHz, $CDCl_3$) of complex **4**.

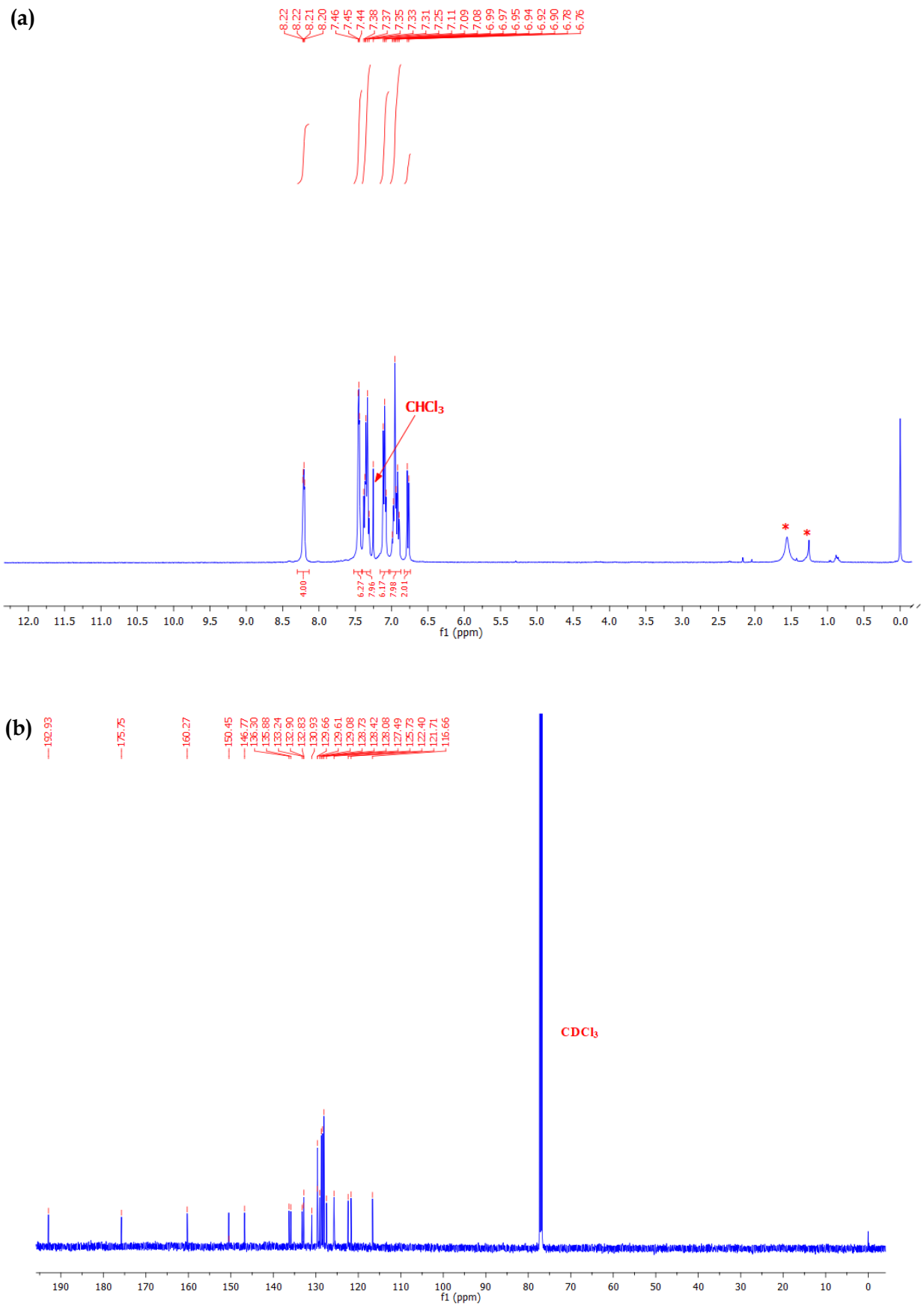


Figure 6.16. (a) ^{1}H NMR (500 MHz, $CDCl_3$) of complex **5**. (b) $^{13}C\{^{1}H\}$ NMR (126 MHz, $CDCl_3$) of complex **5**.

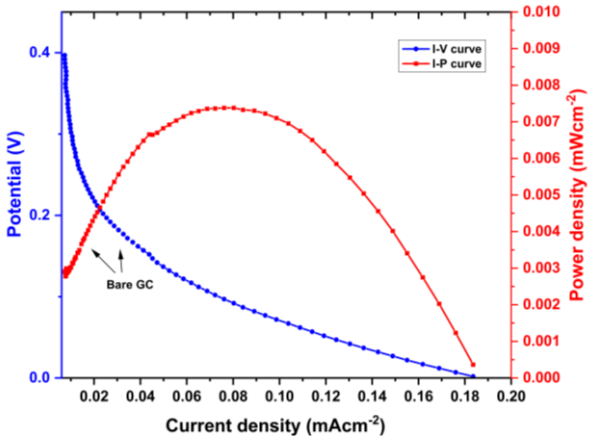


Figure 6.17. I–V(blue) and I–P (red) curves of a single-compartment H_2O_2 fuel cell with Ni anode and bare GC in 0.1 M HCl using 500 mM H_2O_2 with a scan rate of 10 mV s^{-1}.

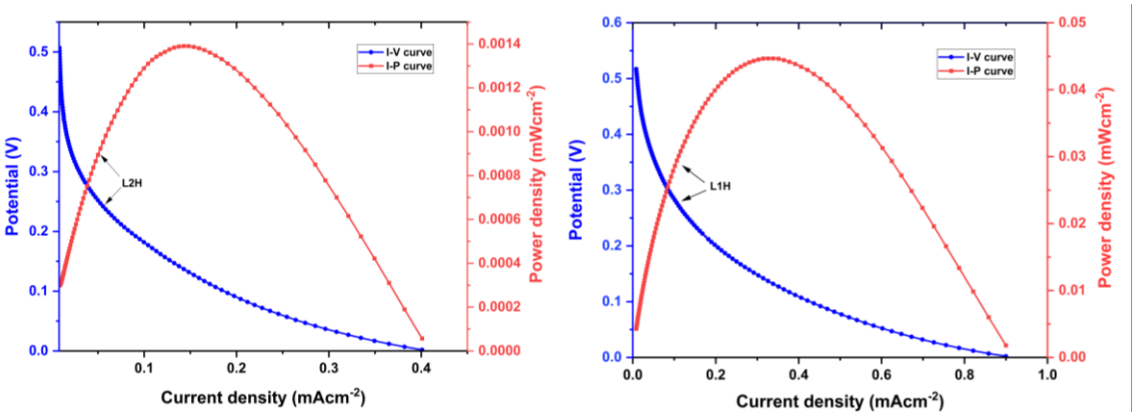


Figure 6.18. I–V(blue) and I–P (red) curves of a single compartment H_2O_2 fuel cell with Ni anode and GC modified with (left) L2H and (right) L1H in 0.1 M HCl using 500 mM H_2O_2 with a scan rate of 10mV s^{-1}.

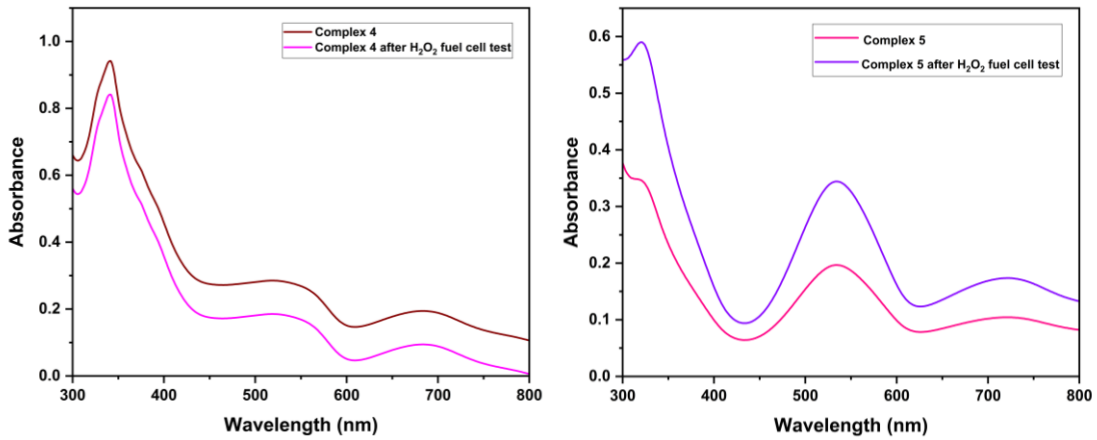


Figure 6.19. UV-vis spectra of (left) complex **4** and (right) complex **5**, and the recovered catalysts after running the H_2O_2 fuel cell test.

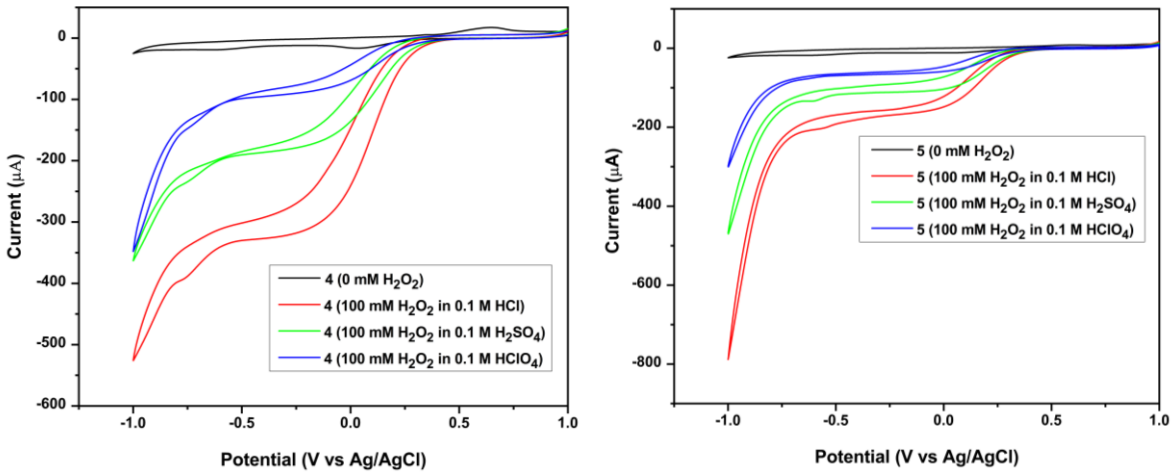


Figure 6.20. CV of H_2O_2 with (left) complex **4** modified electrode and (right) complex **5** modified electrode in 0.1 M HCl (red line), 0.1 M H_2SO_4 (blue line), and 0.1M $HClO_4$ (pink line). CVs using a modified Glassy Carbon electrode as a working electrode in the absence (black line) of H_2O_2 in acetate buffer (pH= 3) are also shown for reference. Ag/AgCl as reference and Pt-wire as a counter electrode are used at a scan rate of 50 mV s^{-1}.

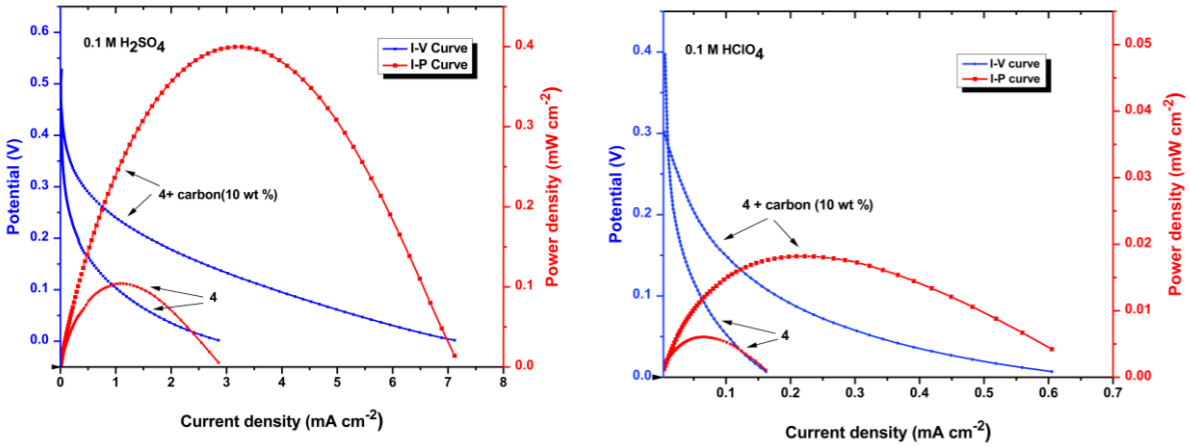


Figure 6.21. I–V(blue) and I–P (red) curves of a single compartment H_2O_2 fuel cell with Ni anode and GC modified with complex **4** in (left) 0.1 M H_2SO_4 and (right) in 0.1 M $HClO_4$ using 500 mM H_2O_2 with a scan rate of 10 mV s^{-1}.

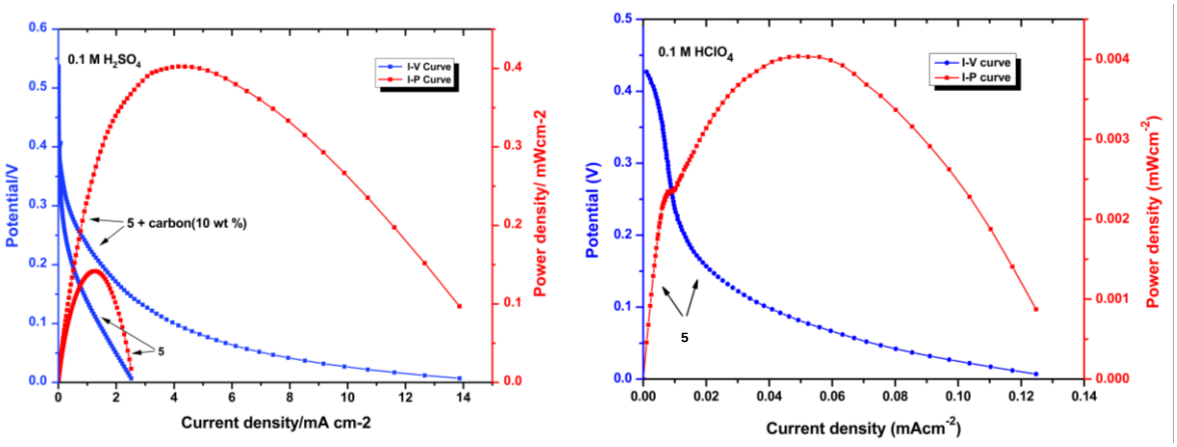


Figure 6.22. I–V(blue) and I–P (red) curves of a single compartment H_2O_2 fuel cell with Ni anode and GC modified with complex **5** in (left) 0.1 M H_2SO_4 and (right) in 0.1 M $HClO_4$ using 500 mM H_2O_2 with a scan rate of 10 mV s^{-1}.

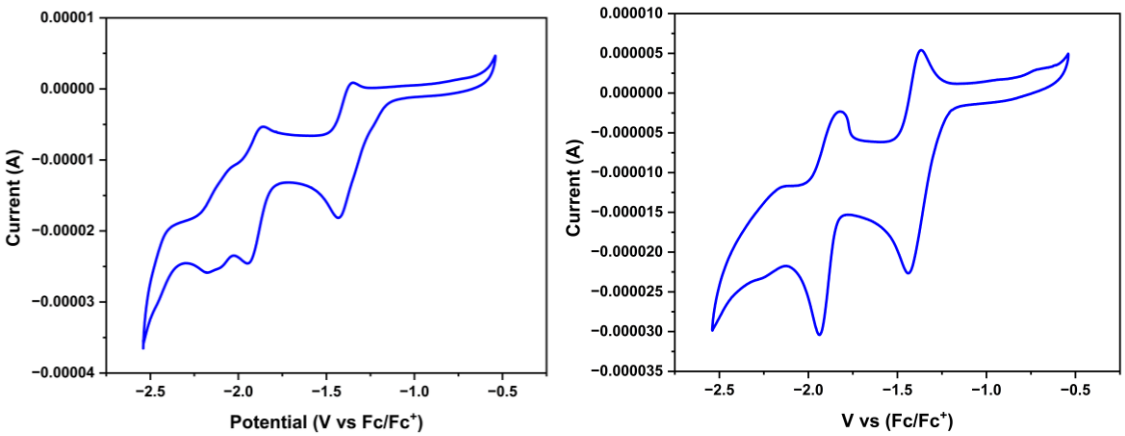


Figure 6.23. Cyclic voltammograms of complex (left) L2H and (right) L1H (1.5 mM solution of ligands in DMF; 0.1 M $[Bu_4N][PF_6]$ electrolyte; scan rate = 10 $mV \cdot s^{-1}$) acquired using a Pt working electrode, Pt-wire counter electrode, and Ag/AgCl (3.0 M KCl) reference electrode.